CHAPTER IV
SYNTHESIS AND CHARATERIZATION OF Fe-Ce-MCM-48 FROM SILATRANE PRECURSOR VIA SOL-GEL PROCESS

4.1 Abstract

A series of Fe (0.01 mole) and Ce (0.01 to 0.09 mole) incorporated into MCM-48 framework was successfully synthesized by sol-gel method using cetyltrimethylammonium bromide (CTAB) as a structural directing agent, silatrane, $FeCl_3$, and cerium glycolate as silica, iron, and cerium sources, respectively. X-ray diffraction (XRD) patterns showed well-defined order cubic mesoporous structures while N_2 adsorption/desorption measurements indicated that the synthesized bimetallic materials had BET surface area up to 1,225 m^2/g, large mesopores (3.1 nm), mean pore volume 0.83 cm^2/g and mean pore diameter 2.89 nm. X-ray fluorescence (XRF) observed the total metal content of final product. UV-visible absorption spectra confirmed that both iron (Fe^{3+}) and cerium (Ce^{4+}) species existed in highly dispersed tetrahedrally coordination in the framework. Scanning electron microscope (SEM) illustrated the truncated octahedron morphology of Fe-Ce-MCM-48.

4.2 Introduction

The mesoporous materials discovered by Mobil group are known as M41S family [1]. These materials can overcome the limitation of microporous materials that cannot allow large reactants to penetrate inside the pores. The main members of the M41S family are hexagonal MCM-41, cubic MCM-48, and unstable lamellar MCM-50 mesostructures. Among them, MCM-48 is the most attractive material owing to its three-dimensional interconnected channels, providing more advantages over one-dimensional pores of MCM-41, such as fast diffusion, resistance to pore blocking of coming molecules, etc. Moreover, due to the long-range order, large surface area, and narrow pore size distribution, MCM-48 is, thus, used as adsorbents, catalyst, catalyst support, sensor, and an inorganic template for the synthesis of advanced nanostructure [2-5]. However, the pure silica MCM-48 is lack of the catalytic active sites, thus, many researchers have attempted to incorporate heteroatoms, such as Fe, Ce, Cr, V, Ti, etc. [6-8] into the mesoporous framework to enhance the redox properties. MCM-48 supporting two or more metal atoms is very attractive since one metal can modify the structural and the redox properties of the other. Consequently, bimetallic catalysts usually improve catalytic activity, selectivity, and stability of the monometallic catalysts. Many reports have shown that Fe-containing materials have high activity in the phenol hydroxylation [6,9] and cerium enhances hydrothermal stability [7,10]. Generally, in catalytic reactions, the catalyst is exposed to high temperature or boiling water, therefore, the loss of hydrothermal stability could be a serious barrier for the application. Simultaneous incorporation of these two metals onto MCM-48 might enhance both phenol hydroxylation and hydrothermal properties. In this study, Fe-Ce-MCM-48 loading different iron and cerium contents was hydrothermally synthesized via sol-gel method and characterized using XRD, XRF, N_2 adsorption/desorption, DRUV, and SEM.

4.3 Experimental

4.3.1 Materials

Fumed silica (99.8%, SiO_2), cerium (IV) hydroxide ($Ce(OH)_4$), and iron (III) chloride hexahydrate ($FeCl_3 \cdot 6H_2O$) from Sigma-Aldich, USA, hexadecyltrimethyl ammonium bromide (CTAB) from Fluka, denmark, triethylenetetramine (TETA) from Facai, Thailand, ethylene glycol (EG) from J.T. Baker, USA), triethanolamine (TEA) from QREC, Asia, acetronitrile and sodium hydroxide (NaOH) from Labscan, Asia, were used without purification.

4.3.2 Synthesis of xFe-yCe-MCM-48

Bimetallic MCM-48 materials were synthesized using Wongkasemjit's method [11]. A desired amount of $FeCl_3 \cdot 6H_2O$ was dissolved in water. The solution was stirred continuously while adding 2 M NaOH. The mixture was then slightly heated at 50 °C while adding CTAB, followed by dissolving silatrane precursor synthesized according to the method described in elsewhere [12]. A required amount of cerium glycolate prepared, following the method in ref. 13, was added and stirred for 1 h. The molar ratio composition of the gel was $1.0SiO_2$:0.3CTAB:0.5NaOH:$62.0H_2O$:xFe:yCe, where $0.01 \leq x, y \leq 0.09$. The mixture was autoclaved for 16 h in a Teflon-lined stainless steel vessel and treated at 140 °C. The resultant solid product was filtered and washed with distilled water. After drying, the sample was calcined at 550 °C for 6 h in air at a heating rate of 0.5 °C/min. Pure MCM-48, Fe-MCM-48, and Ce-MCM-48 were also synthesized, using the same method as the bimetallic MCM-48, for comparison.

4.3.3 Characterization

XRD patterns were recorded on a Rigaku X-ray diffractometer with CuKα radiation over the range of 2θ = 2-6°. XRF was carried out using a

PANalytical AXIOS PW 4400. The N_2 adsorption/desorption was determined by a Quantasorb JR instrument using the Brunauer-Emmett-Teller (BET) method. Diffuse reflectance UV-visible (DRUV) spectra were measured on a Shimadzu UV-2550. SEM micrographs were obtained using a Hitachi S-4800.

4.4 Results and Discussion

4.4.1 XRD

The XRD patterns of the calcined samples shown in Fig. 4.1 indicate that Ce-MCM-48 with Ce/Si molar ratio from 0.01 to 0.09 gave the patterns consistent with the reported MCM-48 in 2θ range of 2–6°, being indexed to the [211], [220], [420], and [332] reflections of the *Ia3d* cubic phase of MCM-48, as compared with JCPDS no. 00-051-1592 [11]. As the contents of heteroatoms increased, all the peaks obviously shifted to lower angles, implying the dilation of material structure. The radii of Ce^{4+} (Paulling radius = 103.4 pm) and Fe^{3+} (Paulling radius = 64 pm) are larger than that of Si^{4+} (Paulling radius = 42 pm), there should be enlargement in the unit cell parameter as the bimetal cations incorporated, resulting in a larger M-O bond distance. This is confirmed by the increase of the *d* spacing of bimetallic materials [14-15]. Mono- and bimetallic MCM-48 containing Fe/Si more than 0.01 molar ratios were not successfully achieved, probably due to imbalance of charge matching [16]. Thus, high Fe/Si ratios could not be synthesized while bimetallic samples of *xFe-yCe-MCM-48* with $x = 0.01$ and $0.01 \leq y \leq 0.07$ provided cubic morphology of MCM-48. According to the study of Zhao *et al.* [17] on the formation of cubic phase using $g = V/a_0 l$, where g is the local effective surfactant packing parameter, V is the volume of hydrophobic tail, a_0 is the effective headgroup area of the cationic ammonium, and l is the kinetic length of the hydrophobic tail of the surfactant, the cubic phase can be easily formed if g is large. The presence of the anionic species of $FeCl_3$ and $Ce(C_2H_4O_2)_2$ metal precursors increases the local effective surfactant packing parameter (g) value, causing the phase change from hexagonal to cubic phases. Moreover, Mahoney [16] also found that the unequal distribution of charge density in the electric double layer resulted in a curvature of

surface in which the cubic structure prefers a high curvature radius with high *g*. A comparison between those two anions, $C_2H_4O_2^{2-}$ and Cl^-, reveals $C_2H_4O_2^{2-}$ to be more effective in reducing the thickness of the double electric layer because of its higher valence state [17]. Therefore, $C_2H_4O_2^{2-}$ is cooperatively assembled better between the ammonium cations and the inorganic silicate anions. From the XRD results, it is clearly seen that the cubic structure of bimetallic products were successfully obtained at various amounts of Ce with the 0.01 Fe/Si molar ratio.

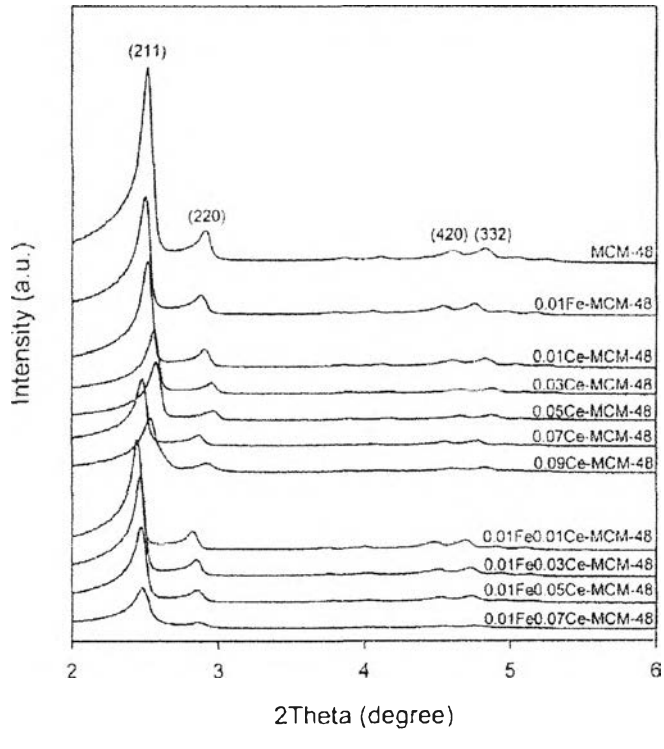

Figure 4.1 XRD patterns of MCM-48, Fe-MCM-48, Ce-MCM-48 and Fe-Ce-MCM-48.

4.4.2 N_2 adsorption/desorption isotherms

The N_2 adsorption/desorption isotherms and pore size distribution curves of the products are shown in Fig. 4.2. All the samples showed a steep increase in the volume of the adsorbed nitrogen at P/P_0 = 0.20–0.35, exhibiting the type IV

isotherm which confirms the mesoporous structure with a narrow pore size distribution, having an average pore size ~2–3 nm. The structural parameters of various samples are summarized in Table 4.1. Comparing with the pure MCM-48, the heteroatom incorporation resulted in higher pore diameter and unit cell (a_0). BET surface area decreased with an increasing amount of incorporated metal. This could be explained by some destruction of metallic MCM-48 pore structure, which is in agreement with the XRD's results [18]. However, high BET surface area over 1000 m^2/g was obtained for all samples.

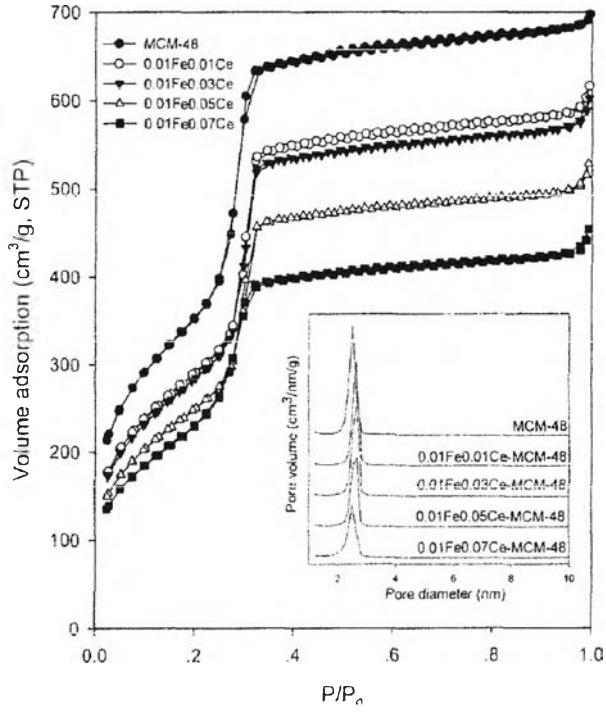

Figure 4.2 N_2 adsorption/desorption isotherms of MCM-48 and Fe-Ce-MCM-48.

4.4.3 XRF spectroscopy

The XRF results (Table 4.1) confirmed the total amount of Fe and Ce that was introduced into MCM-48. However, the actual amount of the metal was less than the added amount due to the solubility of Fe and Ce sources in the medium.

Table 4.1 Textural properties of MCM-48 and metal modified MCM-48

Sample	Fe/Si* (mole ratio)		Ce/Si* (mole ratio)		BET surface area (m^2/g)	pore volume (cm^2/g)	pore diameter (nm)	a_0 [a] (nm)	d_{211} (nm)	wall thickness[b] (nm)
	Gel	Product	Gel	Product						
MCM-48	0	0	0	0	1673	1.07	2.56	8.57	3.50	1.46
0.01Fe-MCM-48	0.01	0.004	0	0	1295	0.98	3.04	8.65	3.53	1.28
0.01Ce-MCM-48	0	0	0.01	0.004	1469	0.91	2.47	8.57	3.50	1.54
0.03Ce-MCM-48	0	0	0.03	0.010	1318	0.82	2.49	8.45	3.45	1.49
0.05Ce-MCM-48	0	0	0.05	0.018	1213	0.76	2.52	8.40	3.43	1.46
0.07Ce-MCM-48	0	0	0.07	0.028	1128	0.76	2.68	8.72	3.56	1.50
0.09Ce-MCM-48	0	0	0.09	0.030	1131	0.74	2.63	8.52	3.48	1.44
0.01Fe-0.01Ce-MCM-48	0.01	0.005	0.01	0.005	1214	0.93	3.07	8.87	3.62	1.33
0.01Fe-0.03Ce-MCM-48	0.01	0.005	0.03	0.014	1225	0.91	2.97	8.77	3.58	1.35
0.01Fe-0.05Ce-MCM-48	0.01	0.004	0.05	0.020	1080	0.80	2.95	8.74	3.57	1.35
0.01Fe-0.07Ce-MCM-48	0.01	0.005	0.07	0.033	1070	0.68	2.55	8.72	3.56	1.55

[a] $a_0 = d_{211}(6)^{1/2}$, [b] Wall thickness = $a_0/3.0919$ – pore diameter/2, * Data were obtained from XRF

4.4.4 DRUV-Vis spectroscopy

DRUV-Vis spectra of the synthesized samples are presented in Fig. 4.3. The absorption band is absent for MCM-48 while Fe-MCM-48 showed a strong absorption at 200 nm, attributed to the charge-transfer transitions involving isolated framework Fe^{3+} in FeO_4 tetrahedral coordination [10]. In addition, there is no absorption band at 500–600 nm, referring to Fe^{3+} octahedral coordination in extraframework [9]. The result suggests that iron indeed exists inside MCM-48 framework. For Ce-MCM-48, they exhibited a weak broad band at 200–300 nm and an intense band at 350 nm. These bands were corresponding to Ce^{4+} tetrahedral coordination. No extraframework band at 405 nm was observed [19]. As the cerium content increased, the band at 350 nm was also increased. Fe-Ce-MCM-48 exhibited iron and cerium bands at 200 and 350 nm, respectively. Both iron and cerium were very well incorporated into MCM-48 framework.

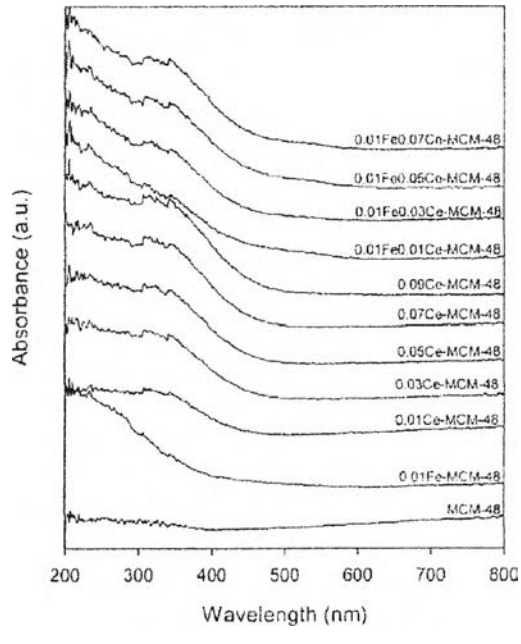

Figure 4.3 DR UV-vis spectra of MCM-48, Fe-MCM-48, Ce-MCM-48 and Fe-Ce-MCM-48.

Table 4.2 Band gap energy of the synthesized metal modified MCM-48

Materials		Wavelength (nm)	Band gap energy (eV)
0.01Fe-MCM-48		418.8	2.960
0.01Ce-MCM-48		465.1	2.665
0.03Ce-MCM-48		466.3	2.658
0.05Ce-MCM-48		467.5	2.651
0.07Ce-MCM-48		485.0	2.556
0.09Ce-MCM-48		489.9	2.53
0.01Fe0.01Ce-MCM-48	Fe	476.4	2.602
	Ce	487.4	2.543
0.01Fe0.03Ce-MCM-48	Fe	473.8	2.616
	Ce	495.1	2.504
0.01Fe0.05Ce-MCM-48	Fe	496.3	2.497
	Ce	516.3	2.401
0.01Fe0.07Ce-MCM-48	Fe	501.3	2.472
	Ce	517.5	2.395

Band gap energy of all samples, calculated from UV-vis spectra, was shown in Table 4.2 (See appendices for calculation). The UV-vis spectra of Ce-MCM-48 shows the red shift as the amount of Ce increased due to the formation of some localized band gap state caused by Ce and oxygen vacancies [22]. The band gap decreased with increasing Ce concentration, which forms some localized gap state in the band gap [22]. For Fe-Ce-MCM-48, the red shift also occurred for Ce and Fe. However, the content of Fe in all bimetallic MCM-48 was constant; thus, the decrease in the band gap was from the concentration of the Ce content.

4.4.5 FE-SEM

SEM images of the samples are shown in Fig. 4.4. Ce-MCM-48 morphology was quite the same as pure MCM-48 because the anionic $C_2H_4O_2^{2-}$

facilitates the formation of the cubic structure. However, in the case of the Cl^- in $FeCl_3$, it does not seem to support the cubic formation, thus, causing more distortion from MCM-48 in the Fe-MCM-48 morphology. Bimetallic Fe-Ce-MCM-48 showed much more distortion since there are two metal atoms and high counterions in the system. Moreover, as the metal contents in bimetallic materials increased, Figures 4.4d-g show a reducing trend in the crystal size. As described by Vekilov and Kashchiev, at high metal ratio, there are more ions in the solution that can form many nuclei, hence causing many tiny crystal growth [20-21].

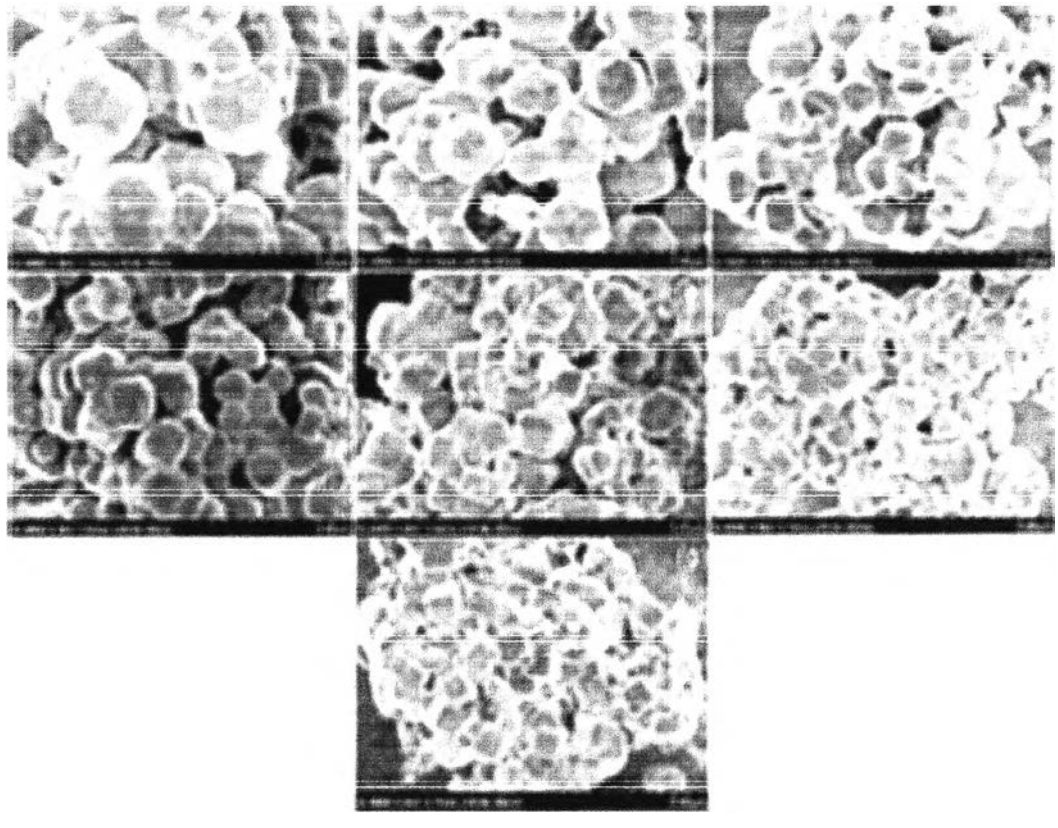

Figure 4.4 FE-SEM images of (a) MCM-48, (b) 0.01Ce-MCM-48, (c) 0.01Fe-MCM-48, (d) 0.01Fe0.01Ce-MCM-48, (e) 0.01Fe0.03Ce-MCM-48, (f) 0.01Fe0.05Ce-MCM-48, (g) 0.01Fe0.07Ce-MCM-48.

4.5 Conclusions

Fe-Ce-MCM-48 mesoporous structures were successfully synthesized using silatrane as a silica source. High iron content in MCM-48 could not be achieved while various amounts of Ce in MCM-48 were well incorporated. Highly dispersion of Fe and Ce in the bimetallic framework at 0.01Fe/Si and various cerium contents (Ce/Si=0.01-0.07) was observed and all synthesized samples provided high surface area and narrow pore size distribution.

4.6 Acknowledgements

This research is financially supported by the Thailand Research Fund, Ratchadapisake Sompote Fund, and the Center of Excellence on Petrochemical and Materials Technology, Chulalongkorn University, Thailand. The authors would like to thank Mr. John M. Jackson for English proofreading.

4.7 References

[1] Kresge CT, Leonowicz ME, Roth WJ, Vartuli JC, Beck JS. Nature 1992; 359: 710-2.

[2] Taguchi A, Schüth F. Microporous Mesoporous Mater 2005; 77: 1-45.

[3] Loger NZ, Kaučič V. Acta Chim Slov 2006; 53: 117-35.

[4] Lysenko ND, Shvets AV, Il'in VG. Theor Exp Chem 2008; 44: 3.

[5] Jiang T, Wu D, Song J, Zhou X, Zhao Q, Ji M, Yin H. Powder Technol 2011; 207: 422-7.

[6] Zhao W, Luo Y, Deng P, Li Q. Catal Lett 2001; 73: 2-4.

[7] Selvaraj M, Park DW, Ha CS. Microporous Mesoporous Mater 2011; 138: 94-101.

[8] Gomes HT, Selvam P, Dapurkar SE, Figueiredo JL, Faria JL. Microporous Mesoporous Mater 2005; 86: 287-94.

[9] Liu H, Lu G, Gao Y, Wang J. Nanotechnology 2006; 17: 997-1003.

[10] Shao Y, Wang L, Zhang J, Anpo M. J Phys Chem B 2005; 109: 20835-41.

[11] Longloilert R, Chaisuwan T, Luengnaruemitchai A, Wongkasemjit S. J Sol-Gel Sci Technol 2011; 58: 427-35.

[12] Charoenpinijkarn W, Suwankruharn M, Kesapabutr B, Wongkasemjit S, Jamieson AM. Eur Polym J 2001; 37: 1441-8.

[13] Ksapabutr B, Gulari E, Wongkasemjit S. Mater Chem Phys 2004; 83: 34-42.

[14] Zhang Y, Gao F, Wan H, Wu C, Kong Y, Wu X, Zhao B, Dong L, Chen Y. Microporous Mesoporous Mater 2008; 113: 393-401.

[15] Rath D, Parida KM. Ind Eng Chem Res 2011; 50: 2839-49.

[16] Mahoney LM. Photocatalysis studies using mesoporous modified V-MCM-48 stober synthesis. Ph.D. Thesis. Kansas state university; 2010.

[17] Zhao W, Kong L, Luo Y, Li Q. Microporous Mesoporous Mater 2007; 100: 111-7.

[18] Ji D, Ren T, Yan L, Suo J. Mat Lett 2003;57 : 4474-7.

[19] Longloilert R, Chaisuwan T, Luengnaruemitchai A, Wongkasemjit S. J Sol-Gel Sci Technol 2012; 61: 133-43.

[20] Vekilov PG. Crys Growth Des 2010; 10:12.

[21] Kashchiev D, Van Rosmalen GM. Cryst Res Technol 2003; 38: 7-8.

[22] M.K. Mahammad, S.A. Ansari, D. Pradhan, D.H. Han, J. Lee, M.H. Cho, Ind. Eng. Chem. Res. 2014; 53: 9754-9763.